ACS Catalysis

pubs.acs.org/acscatalysis

Research Article

# Atomically Dispersed $MnN_4$ Catalysts *via* Environmentally Benign Aqueous Synthesis for Oxygen Reduction: Mechanistic Understanding of Activity and Stability Improvements

Mengjie Chen,[▽] Xing Li,[▽] Fan Yang,[▽] Boyang Li, Thomas Stracensky, Stavros Karakalos, Sanjeev Mukerjee, Qingying Jia, Dong Su, Guofeng Wang,* Gang Wu,* and Hui Xu*

Cite This: *ACS Catal.* 2020, 10, 10523−10534

Read Online

ACCESS | Metrics & More | Article Recommendations | Supporting Information

**ABSTRACT:** Development of platinum group metal (PGM)-free and iron-free catalysts for the kinetically sluggish oxygen reduction reaction (ORR) is crucial for proton-exchange membrane fuel cells. A major challenge is their insufficient performance and durability in the membrane electrode assembly (MEA) under practical hydrogen-air conditions. Herein, we report an effective strategy to synthesize atomically dispersed Mn−N−C catalysts from an environmentally benign aqueous solution, instead of traditional organic solvents. This innovative synthesis method yields an extremely high surface area for accommodating an increased density of $MnN_4$ active sites, which was verified by using advanced electron microscopy and X-ray absorption spectroscopy. The Mn−N−C catalyst exhibits promising ORR activity along with significantly enhanced stability, achieving a peak power density of 0.39 W $cm^{-2}$ under 1.0 bar $H_2$-air condition in a MEA, outperforming most PGM-free ORR catalysts. The improved performance is likely due to the unique catalyst features, including the curved surface morphology and dominant graphitic carbon structure, thus benefiting mass transport and improving stability. The first-principles calculations further elucidate the enhanced stability, suggesting that $MnN_4$ sites have a higher resistance to demetallation than the traditional $FeN_4$ sites during the ORR.

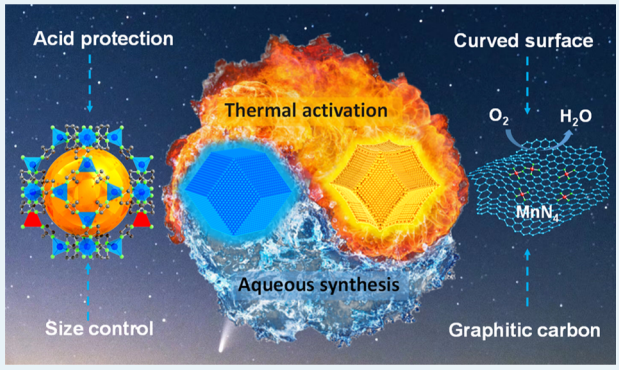


**KEYWORDS:** *PGM-free catalysts, single metal sites, Mn catalysts, electrocatalysis, oxygen reduction*

## 1. INTRODUCTION

Driven by the need to eliminate platinum group metal (PGM) catalysts, the research of PGM-free oxygen reduction reaction (ORR) cathode catalysts for proton-exchange membrane fuel cells (PEMFCs) has made unprecedented progress in the past decade.[1−4] Inspired by pioneering research,[5,6] the carbon-based transition metal−nitrogen−carbon (M−N−C) catalyst (M: Fe, Co, or Mn) holds great promise because of their highly intrinsic activity and reasonable stability in acidic media for the ORR.[1,7,8] Among all M−N−C catalysts, Fe-based catalysts have demonstrated the most promising activity.[9−13] However, the inferior durability of Fe−N−C catalysts in membrane electrode assemblies (MEAs) is still a substantial technical barrier for fuel cell transportation applications. Even worse, the $H_2O_2$ generated during the ORR would react with $Fe^{3+}/Fe^{2+}$ to form detrimental hydroxyl and hydroperoxyl radicals *via* Fenton reactions, which attack organic ionomers, membranes, and catalysts.[14−16] Eventually, the severe performance loss and cell failure occur because of the chemical and mechanical degradation of MEAs.[17] Therefore, the Fe-based catalyst is not ideal for replacing PGM catalysts in PEMFCs.[14,18] Although Co−N−C catalysts can alleviate the Fenton reactions to a certain degree, their relatively low intrinsic activity and high cost remain grand challenges.[19] Therefore, Mn-N-C catalysts, which are low cost and have negligible activity toward the Fenton reactions, are highly desirable PGM-free catalysts. In our previous works, we had experimentally and theoretically explored the effectiveness to generate a high density of $MnN_4$ active sites embedded in a carbon phase, exhibiting promising catalytic activity and stability.[20,21] However, the Mn−N−C catalyst showed limited performance in a practical $H_2$-air fuel cell test with a low power density of 0.18 W $cm^{-2}$ under the practical air condition, which was far less than that of benchmark Fe−N−C catalysts.[22−24]

Received: June 5, 2020
Revised: August 10, 2020
Published: September 3, 2020

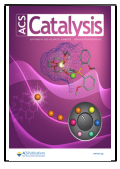









https://dx.doi.org/10.1021/acscatal.0c02490
*ACS Catal.* 2020, 10, 10523−10534

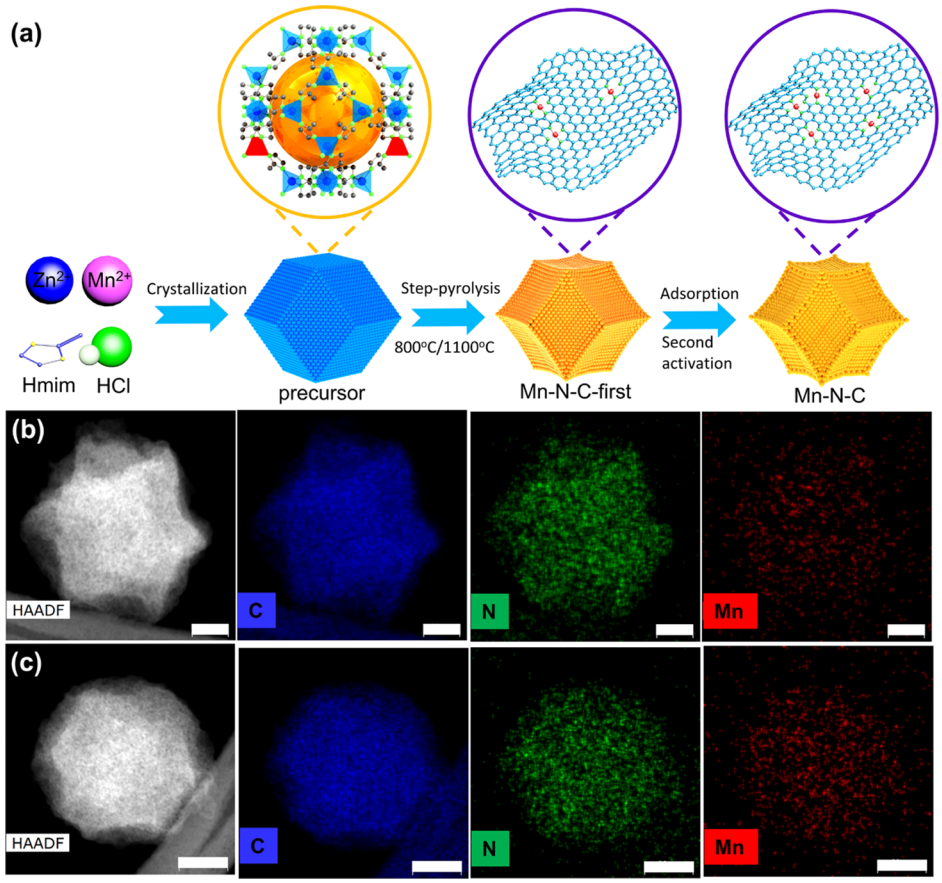


**Figure 1.** (a) Aqueous synthesis scheme for Mn−N−C catalysts and HAADF-STEM images with corresponding EDS elemental mappings of C, N, and Mn for (b) Mn−N−C−HCl-800/1100-first catalyst (scan bar: 20 nm) and (c) Mn−N−C−HCl-800/1100 catalyst after the second adsorption to introduce additional $MnN_4$ sites (scan bar: 30 nm).

The atomic $MN_4$ moieties, which are generally dispersed and embedded in micropores, are identified as ORR active sites, as proven by advanced spectroscopic characterizations and first-principles calculations.[25,26] Similar to most of the other M−N−C catalysts, current Mn−N−C catalysts are derived from zinc-based zeolitic imidazolate frameworks (ZIF-8s), a subfamily of metal−organic frameworks.[27] Because ZIF-8-derived carbon materials synthesized *via* carbonization at high temperature (*e.g.*, 1100 °C) possess an abundance of micropores and defects,[28,29] which are favorable for hosting a high density of $MnN_4$ sites with atomic dispersion in carbon. However, most of the ZIF-8 crystal precursors are prepared from organic solvents such as methanol and dimethylformamide (DMF).[30,31] These organic solvents are toxic, costly, and potentially harmful to the environment, thus contradicting the sustainable concept of developing PGM-free catalysts for clean energy. Some reports have tried to circumvent this issue *via* solid-state synthesis of ZIF-8.[32] These materials suffer from complicated procedures and heterogeneous morphology. In contrast, the synthesis of ZIF-8 in aqueous solutions would have many advantages including high efficiency, low cost, and being environmentally friendly.[33]

Herein, we have developed a highly active Mn−N−C cathode catalyst from an aqueous solution synthesis method by using an acid-assisted step-pyrolysis strategy. This catalyst exhibits significantly enhanced activity and fuel cell performance, dramatically outperforming our previous Mn−N−C catalysts in 2018 by using DMF synthesis methods.[20] The new Mn−N−C catalyst achieved remarkable MEA performance, that is, the peak power density of 0.39 W $cm^{-2}$ under $H_2$-air. The homogeneous atomically dispersed $MnN_4$ active sites were directly confirmed by X-ray absorption spectroscopy (XAS) and high-resolution-scanning transmission electron microscopy (HR-STEM) images along with electron energy loss spectroscopy (EELS). This aqueous synthesis method yielded predominantly microporous carbon structures with extremely high surface area (> 1500 $m^2$ $g^{-1}$) and a unique curved surface morphology, which is beneficial for hosting $MnN_4$ moieties and improving mass transport. Enhanced stability was also achieved because of the robust nature of $MnN_4$ and the formation of a graphitic carbon structure with a high degree of curvature. Compared to $FeN_4$, the higher resistance for metal leaching of $MnN_4$ moieties was further confirmed by density functional theory (DFT) calculations. Hence, this work provided a new concept to develop atomically dispersed single metal site catalysts by using environmentally friendly aqueous synthesis with improved catalyst performance relative to traditional organic solvent-based synthesis.

## 2. RESULTS AND DISCUSSION

**2.1. Catalyst Synthesis, Structures, and Morphologies.** Three different catalyst samples were synthesized and studied in this work (details can be found in the Supporting Information). Typically, Mn-doped ZIF-8 precursors were prepared and carbonized from different procedures. For the


https://dx.doi.org/10.1021/acscatal.0c02490
ACS Catal. 2020, 10, 10523−10534

Mn−N−C-1100 catalyst, the precursors were synthesized in the absence of acid protection in an aqueous solution and heat-treated at 1100 °C (the first thermal activation), followed by adsorption procedure and second thermal activation. For the Mn−N−C−HCl-1100 catalyst, the precursors were synthesized with the addition of acid and the rest procedures are identical. For the Mn−N−C−HCl-800/1100 catalyst, the precursors were synthesized with the addition of acid and carbonized from a two step-pyrolysis method, which involved holding the temperature at 800 °C for 2 h and then elevate to 1100 °C for 1 h (the first thermal activation), followed by the same adsorption and a second thermal activation process. During the multiple-step synthesis, Mn−N−C catalysts prepared by the first thermal activation are labeled correspondingly as Mn−N−C-1100-first, Mn−N−C−HCl-1100-first, Mn−N−C−HCl-800/1100-first.

The novel aqueous catalyst synthesis is shown in Figure 1a. The initial Mn-doped ZIF-8 precursors were synthesized in a dilute HCl acid. One of the grand challenges for Mn−N−C catalyst synthesis is that Mn atoms tend to form inactive metallic compounds and oxides, instead of active single metal sites coordinated with N ligands.[20,27] The addition of HCl acid mitigates the hydrolysis process, prevents the formation of manganese oxides/clusters, and generates more porous structures. Moreover, the aqueous synthesis can significantly shorten the reaction time to form ZIF-8 crystals because their nucleation and crystallization rates in water are much faster than those in organic solvents. Based on the X-ray diffraction (XRD) pattern (Figure S1a), the crystal structure of the Mn-doped ZIF-8 precursor was similar to that of reported ZIF-8s,[11,34] further verifying the effectiveness of the aqueous solution to form well-defined ZIF-8 crystals. Next, the Mn-doped ZIF-8 precursors can be carbonized to create a porous carbon structure by evaporating zinc easily, and $MnN_4$ can be created *via* a high-temperature treatment. Thus, the subsequent thermal activation process has a profound effect on the activity of the ZIF-derived Mn−N−C catalysts. A step-pyrolysis strategy (*i.e.*, 800 and 1100 °C) was developed to significantly increase the density of active sites located in the micropores. For example, if the temperature is directly increased to 1100 °C skipping the intermediate 800 °C step, a loss of $MnN_4$ sites occurs because of the collapse of the micropores. As shown in Figure S2, the specific surface area of different catalysts follows this trend: Mn−N−C−HCl-800/1100-first > Mn−N−C−HCl-1100-first > Mn−N−C-1100-first, implying that the acid-assisted step-pyrolysis method can effectively increase the surface area. The Mn−N−C−HCl-800/1100-first catalyst exhibited higher micropore volume within a broader range than the other two catalysts because of less micropore collapse.

The XRD patterns of the obtained catalyst show dominant peaks around 25 and 44°, which can be assigned to carbon planes (002) and (101), respectively (Figure S1b),[35] suggesting that the Mn-doped ZIF-8 precursors are well-carbonized. Unlike the smooth surface often observed in catalysts from organic synthesis,[16,20,34] the curved-surface polyhedron morphology of carbon particles is apparent in the catalyst obtained from the aqueous synthesis method (Figures 1b and S3). The curved surface morphology was created by the anisotropic thermal shrinkage of ZIF-8, where the vertices of the polyhedron are less stressed than the planar faces.[9] Compared to organic solvents used for the synthesis, the much faster crystallization process in the aqueous solvent leads to the formation of more defects, for example, the absence of nodes or linkers.[36] Thus, additional pore sizes are observed in the framework architecture and provide more space for the shrinkage of the ZIF-8 crystal.[37] Consequently, the edge frame of the polyhedron is retained while the planar faces collapse. The curved surface structure may improve the utilization of active sites at the surface by increasing the external surface area and exposing more active sites. It can also facilitate the mass transport by generating more mesopores and macropores.[9,38,39] To further increase the density of active sites, adsorption of Mn ions was performed on the Mn−N−C−HCl-800/1100-first catalyst followed by a second thermal activation. Unlike traditional Fe- or Co-based catalysts, the Mn-based catalysts are very likely to form clusters during the one-step chemical doping, thus generating a very low density of $MnN_4$ active sites. To address this issue, we developed an effective two-step doping and adsorption method to introduce more active Mn sites into carbon catalysts step by step. The unique microporous structure and the richness of nitrogen dopants of ZIF-derived carbon after the first step serve as an ideal host to adsorb Mn ions sites in the second adsorption step and form more $MnN_4$ sites. The STEM−energy dispersive spectroscopy (EDS) elemental mapping shown in Figure 1b,c indicates that C, N, and Mn atoms are uniformly dispersed in the Mn−N−C−HCl-800/1100 catalyst. Notably, compared with the Mn−N−C−HCl-800/1100-first catalyst, the Mn signals became much denser and stronger in the final Mn−N−C−HCl-800/1100 catalyst, suggesting that the adsorption and second thermal activation step can considerably increase the density of $MnN_4$ sites.

**2.2. ORR Activity and Stability.** The ORR activity and selectivity of these catalysts were evaluated by using a rotating ring-disk electrode in 0.5 M $H_2SO_4$ electrolyte at room temperature. The lower activity was observed for Mn−N−C catalysts derived from methanol and DMF, suggesting a much less density of active $MnN_4$ moieties in these catalysts (Figure S4), as the Mn ions cannot be chemically doped into ZIF crystals easily. Unlike traditional organic solvents, in which the Mn ions cannot coordinate with N ligands effectively during the chemical doping step, the Mn−N−C−HCl-800/1100-first catalyst derived from direct Mn-doped ZIF-8 in aqueous solution showed a more positive half-wave potential ($E_{1/2}$) of 0.69 V versus RHE in 0.5 M $H_2SO_4$. $H_2O$ molecules would partially break the coordination bonds between organic linkers and zinc nodes during nucleation and crystallization, exposing the unsaturated N sites for bonding with Mn ions.[40] Thus, more Mn ions can be coordinated with N sites to obtain a higher density of $Mn−N_4$ complexes in aqueous solution.

Notably, zinc in ZIF-8 precursors starts to evaporate under 800 °C to generate a porous structure.[10] Therefore, we chose 800 °C as the critical temperature for the carbonization of Mn-doped ZIF-8 precursors in the first period of the step-pyrolysis process. The poor RDE ORR activity (Figure S5) indicates that there is no formation of $MnN_4$ active sites during the first period of step-pyrolysis. However, after the first period of step-pyrolysis, nitrogen defects were exposed because of zinc evaporation. Then, the temperature was further elevated to 1100 °C to facilitate the diffusion of Mn ions and the generation of $MnN_4$ active sites. Followed by adsorption and the second thermal activation, the Mn−N−C−HCl-800/1100 catalyst showed significantly enhanced activity compared with Mn−N−C−HCl-800/1100-first, proving that more accessible active sites were generated (Figure 2a). This activity


https://dx.doi.org/10.1021/acscatal.0c02490
ACS Catal. 2020, 10, 10523−10534

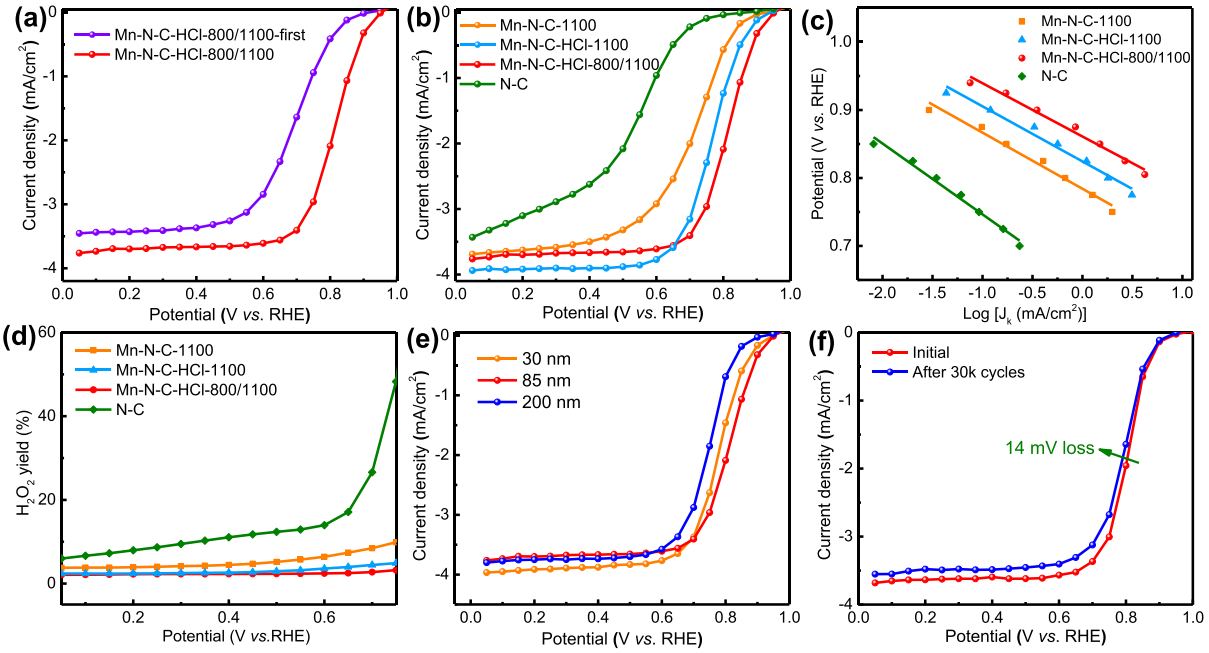


**Figure 2.** (a) Steady-state ORR polarization curves of Mn−N−C−HCl-800/1100-first and Mn−N−C−HCl-800/1100. (b) Steady-state ORR polarization curves of Mn−N−C-1100, Mn−N−C−HCl-1100, Mn−N−C−HCl-800/1100, and N−C. (c) Tafel plots of ORR on different catalysts replotted from the polarization curves. (d) Hydrogen peroxide yields of Mn−N−C-1100, Mn−N−C−HCl-1100, Mn−N−C−HCl-800/1100, and N−C. (e) Steady-state ORR polarization curves of Mn−N−C catalysts with various particle sizes. (f) Steady-state ORR polarization curves of Mn−N−C−HCl-800/1100 before and after potential cycling tests (0.6−1.0 V, 30,000 cycles).

improvement is in good agreement with the results of STEM−EDS mapping showing an increased atomic Mn signal in the final catalyst. The adsorption and the second thermal activation steps can dramatically improve the activity for all Mn catalysts regardless the acid addition and step pyrolysis procedures (Figure S6).

As shown in Figure 2b, the Mn−N−C-1100 catalyst synthesized without the assistance of the acid exhibited inferior ORR activity because of the formation of manganese oxides (Figure S7), which undermined the surface area (Figure S8 and Table S1) and inhibited the formation of $MnN_4$ active sites. With acid assistance, no manganese oxides/clusters are detected in the Mn−N−C−HCl-1100 catalyst, indicating that the acid plays a crucial role in isolating the Mn ions and avoiding the formation of manganese oxides. The best performing Mn−N−C−HCl-800/1100 catalyst showed the highest activity with an $E_{1/2}$ of 0.815 V versus RHE as well as the highest surface area (>1500 $m^2$ $g^{-1}$). The micropore area is the principal key factor in improving ORR activity by accommodating active sites.[41−43] Therefore, the abundant micropores (0.52 $cm^3$ $g^{-1}$) in the Mn−N−C−HCl-800/1100 catalyst is favorable for hosting a high density of active sites. The previously reported 20Mn−NC-second catalyst[20] was compared with our new Mn−N−C−HCl-800/1100 catalyst (Figure S9). The Mn−N−C−HCl-800/1100 catalyst exhibited a current density higher by three times than that of the 20Mn−NC-second catalyst at 0.9 V. Given that less Mn content was observed for the Mn−N−C−HCl-800/1100 catalyst (Table S2), the higher activity can be attributed to the higher utilization of $MnN_4$ moieties at the surface because of the unique curved-surface structure. The activity of the Mn-free nitrogen-doped carbon (N−C) catalyst was also tested under the same condition, which only showed an $E_{1/2}$ around 0.53 V (Figure 2b), suggesting that the formation of Mn-related active sites is essential for the improved ORR activity. As shown in Figure 2c and Table S3, Tafel slopes ranging from 75 to 85 mV $dec^{-1}$ were determined for Mn-based catalysts, suggesting that the mixed control on the rate-determining step involves the transfer of the first electron (118 mV $dec^{-1}$) and the diffusion of intermediates at catalyst surfaces (59 mV $dec^{-1}$).[44−46] Among all Mn−N−C catalysts, the Mn−N−C−HCl-800/1100 catalyst showed the lowest Tafel slope, likely indicating the fastest ORR kinetics. The Mn-free nitrogen-doped carbon catalyst demonstrated a much higher Tafel slope (104 mV $dec^{-1}$) at low currents, suggesting a different reaction mechanism and slower kinetics. Moreover, the Mn−N−C−HCl-800/1100 catalyst yielded insignificant hydrogen peroxides (less than 3%) during the ORR with dominant selectivity of the four-electron pathway (Figure 2d). In this study, Mn−N−C−HCl-800/1100 catalysts with different particle sizes were also prepared and compared, in which the 85 nm catalyst demonstrated the highest activity (Figure 2e). This can be attributed to the highest microporosity and specific surface area observed for the 85 nm catalyst, which in turn facilitated the exposure and utilization of active sites.

Stability of Mn-based catalysts was evaluated *via* accelerated stress tests (potential cycling from 0.6 to 1.0 V) in $O_2$-saturated 0.5 M $H_2SO_4$ during the ORR. The best performing Mn−N−C−HCl-800/1100 catalyst demonstrated excellent stability with a loss of only 14 mV in $E_{1/2}$ after 30,000 cycles (Figure 2f). The stability is significantly enhanced when compared to other ZIF-8 derived Fe−N−C and Co−N−C catalysts,[11,15,16] indicating the Mn−N−C catalyst holds promise to address the stability issue of PGM-free ORR catalysts. For a comparison, the Mn−N−C−HCl-1100 catalyst (without step-pyrolysis) was subject to the identical stability test. The Mn−N−C−HCl-1100 catalyst was found to be less stable (a loss of 43 mV) (Figure S10), suggesting that the step-


https://dx.doi.org/10.1021/acscatal.0c02490
ACS Catal. 2020, 10, 10523−10534

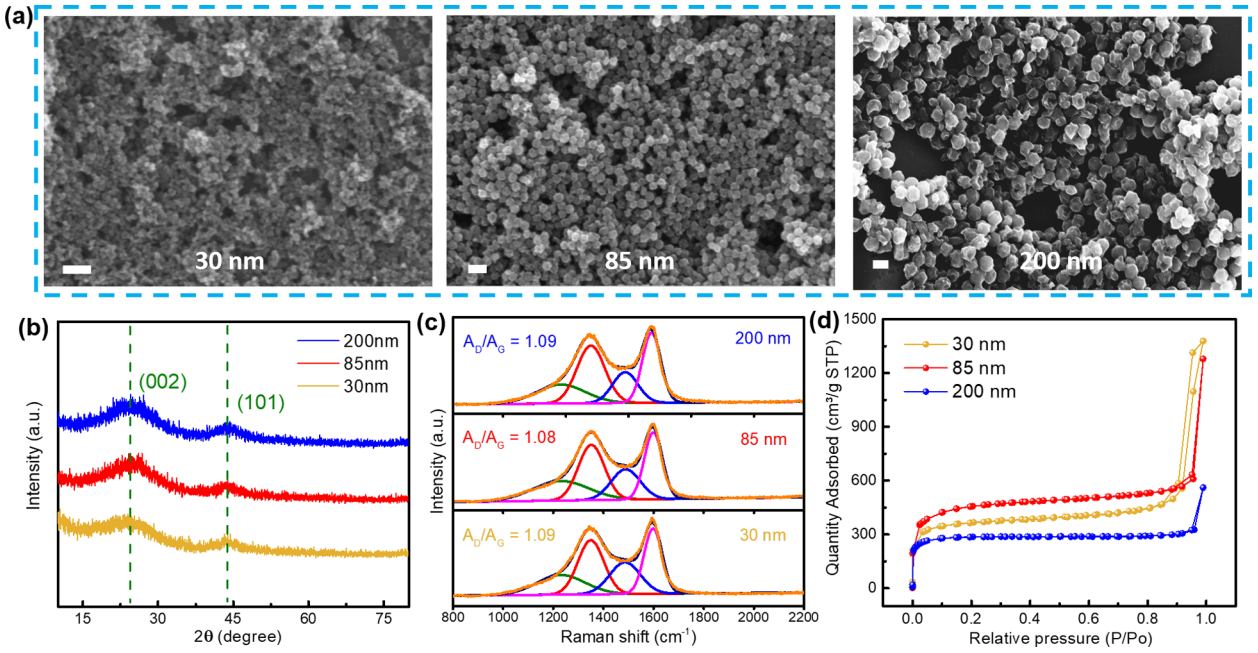


**Figure 3.** (a) Scanning electron microscopy images (scan bar: 200 nm), (b) XRD patterns, (c) Raman spectra, and (d) $N_2$ adsorption/desorption isotherms of Mn−N−C catalysts with various particle sizes.

pyrolysis strategy can improve stability by modifying the carbon structure. Compared with the individual 1100 °C treatment, the Mn−N−C−HCl-800/1100 catalyst demonstrated a smaller increase of capacitance in $H_2SO_4$ solution after the AST, which is due to a more graphitic carbon structure from the longer duration of heat-treatment and modulated temperatures (Figure S11).

**2.3. Mechanistic Understanding of Activity and Stability Improvements.** The ORR activity dependence on the catalyst size was investigated and is shown in Figure 3. Herein, as shown in Figure S12, the size of Mn-doped ZIF precursors was tuned through varying the concentration of zinc ions and 2-methylimidazole. Thus, the particle size of various catalysts can be prepared. After the carbonization, the dominant rhombic polyhedron shape of Mn-doped ZIF-8 was nearly retained except that the catalyst particle was shrunk, and the particle surface became curved. Following the adsorption and the second thermal activation, the catalyst maintained a similar size as it was in the first step (Figure 3a). XRD results indicate all Mn−N−C catalysts showed a similar crystal carbon structure (Figure 3b). From the Raman spectra (Figure 3c), all catalysts also exhibited similar ratios of D and G peak areas ($Area_D/Area_G$), where can be an indicator of the graphitization degree of the carbon structure.[47,48] The $N_2$ adsorption/desorption isotherms (Figure 3d) of the various Mn−N−C catalysts, used to determine the Brunauer−Emmett−Teller (BET) surface areas, provide a discerning factor for catalytic activity. As shown in Figure 2e, the catalytic activity of Mn catalysts follows a trend: 85 > 30 > 200 nm, which is consistent with the trend of specific surface area. The high surface area can be mainly ascribed to the dominant microporosity, evidenced by the gradual increase in the $N_2$ uptake at low pressures. The best performing 85 nm catalyst exhibited the highest surface area (1511 $m^2\ g^{-1}$). The 200 nm catalyst demonstrated the lowest activity with a surface area of 923 $m^2\ g^{-1}$. The catalytic activity, surface areas, and particle sizes are well-correlated in Figure S13 and Table S4.

The atomic-level structure and the chemistry of Mn−N−C catalysts were extensively studied by using high-angle annular dark-field (HAADF)-STEM images, EELS, and XAS analysis. Figure 4a elucidated the overall morphology *via* a STEM image, and the Mn−N−C−HCl-800/1100-first catalyst exhibited a curved surface of polyhedron particles. Figure 4b further showed the porous structure of the Mn−N−C−HCl-800/1100-first catalyst. The nitrogen-coordinated Mn sites (the bright dots in the red circles) can be visualized by using HAADF-STEM (Figure 4c) along with EELS (Figure 4d). The advanced electron microscopy study verifies that atomically dispersed Mn sites are homogeneously embedded into the carbon matrix throughout the catalyst.

Furthermore, the Mn−N−C−HCl-800/1100-first catalyst was subject to an adsorption step and a second thermal activation, where the acid and urea were introduced to prevent the formation of Mn oxides/clusters and provide a source of additional nitrogen, respectively. Moreover, the hydrochloric acid can also activate the catalyst by improving the BET surface area and pore volume of carbon.[49,50] HR-TEM images with electron diffraction patterns (Figure S14) confirm the existence of porous carbon structure, and the absence of Mn oxides or clusters in the catalysts, which are in good agreement with XRD results. Also, compared to the Mn−N−C−HCl-800/1100-first, the curved surface morphology of the Mn−N−C−HCl-800/1100 catalyst became more dominant (Figure 4e), and a more porous structure was achieved (Figures 4f and S15). The increased surface area can be attributed to the fact that the more dominant micropores formed after the adsorption and the second thermal activation (Figure S16), which is related to the pore formation induced by the uses of HCl and urea.[49,51] This is different from the results we observed previously, in which the specific surface area of catalysts was often reduced after the second thermal activation.[20] The higher micropore volume can accommodate more $MnN_4$ active sites in the second step, which has been verified by ORR activity enhancement and STEM elemental


https://dx.doi.org/10.1021/acscatal.0c02490
ACS Catal. 2020, 10, 10523−10534

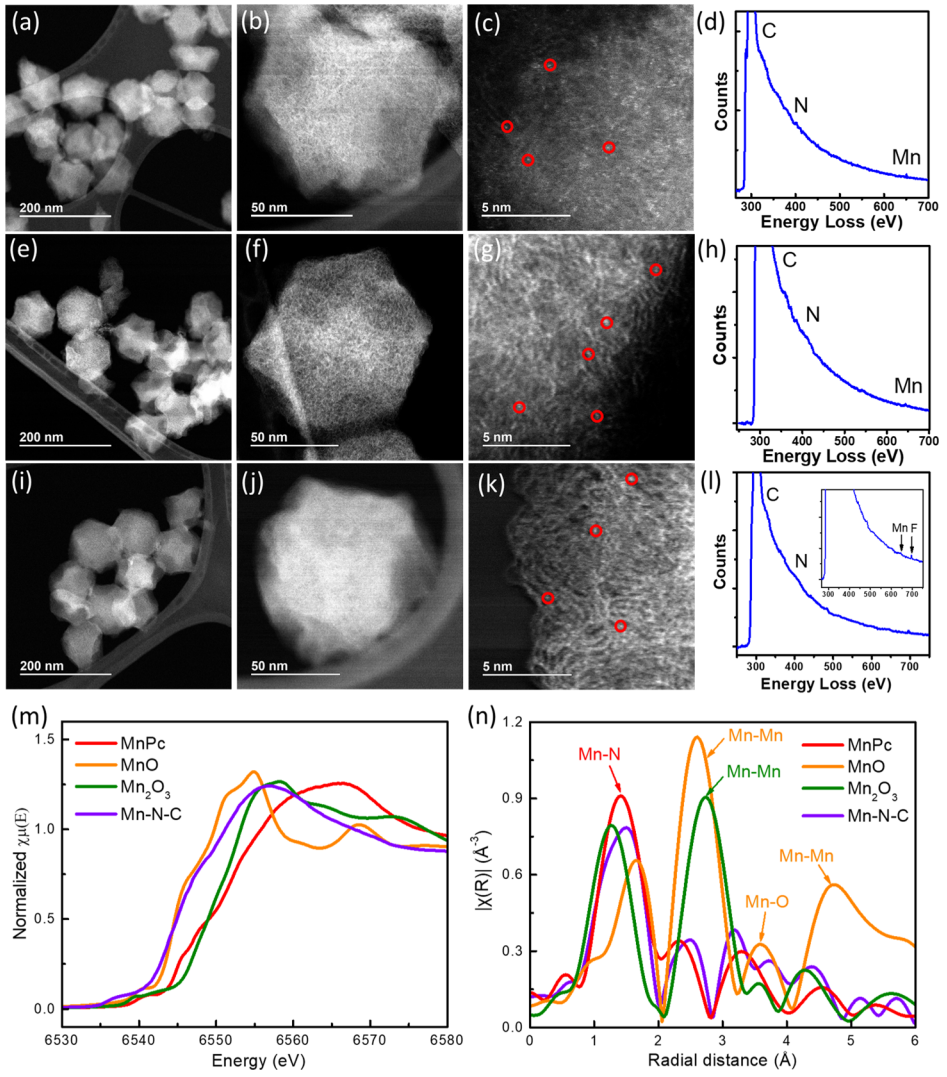


**Figure 4.** STEM images and corresponding EELS of (a–d) Mn–N–C–HCl-800/1100-first, (e–h) Mn–N–C–HCl-800/1100, and (i–l) Mn–N–C–HCl-800/1100 after potential cycling (0.6–1.0 V, 30,000 cycles). (m) K-edge XANES spectra and (n) FT-EXAFS spectra of the Mn–N–C–HCl-800/1100 catalyst and standard samples (MnPc, MnO, and $Mn_2O_3$).

mapping (Figures 1 and 2a). The ammonia generated from the decomposition of urea could help to create more defects, thus increasing the density of $MnN_4$ sites.[26] The atomically dispersed nitrogen-coordinated Mn sites (the bright dots in red circles) in the final catalyst were also verified *via* HR-STEM (Figure 4g) and EELS (Figure 4h). Therefore, the improved ORR activity is due to increased surface area and density of $MnN_4$ active sites.

The best performing Mn–N–C–HCl-800/1100 catalyst after the AST was further studied by using HAADF-STEM, and the images provide an underlying mechanistic understanding of stability enhancement (Figures 4i–l and S17). The carbon's curved surface architecture was retained after 30,000 potential cycles, suggesting excellent stability of the catalyst in terms of carbon corrosion resistance. The carbon stability can be attributed to the formation of a curvature-shaped graphitic carbon structure (Figure S18).[52,53] These graphitic carbon layers stacked in the Mn–N–C–HCl-800/1100 catalyst is possibly related to the step-pyrolysis method and further enhanced by the second thermal activation (Figure S19). The generation of such a high curvature graphitic carbon structure starts from 800 °C during the first period of the step-pyrolysis of the Mn-doped ZIF-8 precursor.[54] Notably, in traditional synthesis methods, the heat-treatment duration is usually short. Therefore, the carbonization of the precursor is insufficient to generate such a graphitic carbon structure. In this work, longer duration of heat treatments, modulated temperature, and additional second thermal activation all facilitate the formation of such unique graphitic carbon structures. After potential cycling, the atomically dispersed nitrogen-coordinated Mn sites were still retained in the carbon matrix, and no Mn clusters were observed, demonstrating the robustness of the Mn–N coordination structure during the ORR in the acid media (Figure 4k,l). This result is consistent with RDE measurements, showing compelling stability enhancment.

In X-ray photoelectron spectroscopy (XPS) analysis, the N 1s peak can be fitted into four peaks situated at 398.3, 399.3, 401.3, and 404.0 eV, which can be assigned to pyridinic-N, Mn–N species, graphitic-N, and oxidized-N, respectively. The nitrogen content and types are similar to traditional Fe-N-C catalysts (Table S2). The pyridinic nitrogen can act as anchor sites to coordinate with Mn sites. Moreover, the graphitic nitrogen was the dominant species observed in our catalysts, which can modify the electronic structure of carbon materials


https://dx.doi.org/10.1021/acscatal.0c02490
ACS Catal. 2020, 10, 10523–10534

by delocalizing the electron distribution of carbon planes to improve the ORR kinetics.[55] Moreover, the d-orbital filling and spin of transition metal center can be significantly impacted by surrounding graphitic N, leading to improved intrinsic activity of $MN_4$ sites.[56] XAS measurements further examined the Mn−N−C catalyst. Manganese phthalocyanine (MnPc), MnO, and $Mn_2O_3$ were also studied as standard Mn compounds for comparison. The bulk average oxidation state of the Mn in the Mn−N−C−HCl-800/1100 catalyst was estimated by the position of the X-ray absorption near-edge structure (XANES) spectra. Figure 4m shows that the edge position of the Mn K-edge XANES spectrum of the Mn−N−C−HCl-800/1100 catalyst nearly overlaps that of the MnO, indicating a bulk average oxidation state of +2. This is in good agreement with the XPS result (Figure S20), where the valence of Mn ions of the Mn−N−C−HCl-800/1100 catalyst was identified to be $Mn^{2+}$ based on the binding energy of Mn $2p_{1/2}$ and Mn $2p_{3/2}$ situated at *ca.* 653.2 and 641.5 eV, respectively. The local structures of Mn sites in the Mn−N−C−HCl-800/1100 catalyst and standard Mn compounds were also characterized by an extended X-ray absorption fine structure (EXAFS) analysis. The Fourier-transformed (FT)-EXAFS spectrum of the Mn−N−C−HCl-800/1100 exhibited a predominant peak of around 1.5 Å (Figure 4n), which can be attributed to the Mn−N/O first coordination shell.[20,57] The two scattering peaks of the MnO around 2.6 and 4.8 Å can be assigned to the Mn−Mn pathways.[58] Thus, the absence of such Mn−Mn peaks for the Mn−N−C−HCl-800/1100 indicates no Mn oxides cluster with long-range ordered structures. The EXAFS analysis agrees with the XRD and STEM results that the Mn exists as atomically dispersed single Mn site species. To further understand the chemical structure of Mn−N coordination, we characterized MnPc with a fingerprint $MnN_4$ structure as a standard baseline for possible active site identification of the Mn−N−C catalyst (Figure S21 and Table S5). It is noted that the FT-EXAFS of the Mn−N−C catalyst closely follows that of the MnPc up to 5 Å (Figure 4n), suggesting the presence of $MnN_4$ moieties in the catalyst. The presence of Mn−O species cannot be conclusively excluded by XAS analysis because N and O as scattering neighbors cannot be distinguished by XAS, but the N coordination is supported by STEM and EELS analysis.

In previous studies,[20,21] we employed the first-principles DFT calculations to predict the intrinsic ORR activity of an $MnN_4$ site. The most likely active site contains a central Mn atom coordinated with four N atoms embedded in a graphene layer with a planar configuration. The $MnN_4$ site exhibits a thermodynamically favorable four-electron pathway for the ORR with a predicted limiting potential of 0.54 V and kinetically feasible activation energy of 0.37 eV for breaking the O−O bond during the OOH dissociation. Hence, these computational results well-explained the observed activity of the Mn−N−C catalysts for the ORR. Here, we further performed the DFT calculations to model the metal leaching processes from both $MnN_4$ and $FeN_4$ sites to attain an understanding of the observed stability improvement of the Mn−N−C catalyst. Calculated Pourbaix diagrams show that these clean $MnN_4$ and $FeN_4$ sites are thermodynamically stable only under low electrode potential ($U < 0.5$ V *vs* RHE) in acid media.[59] Under electrode potentials higher than 0.5 V, the $MnN_4$ site was predicted to be terminated by an oxygen atom, whereas the $FeN_4$ site terminated by a hydroxyl group. The different stable states of the $MnN_4$ and $FeN_4$ sites during ORR at high potential is a result of the lower thermodynamic driving force for O protonation reaction to form OH on $MnN_4$ than on $FeN_4$ site. The adsorption of an oxygen molecule ($O_2$) on the central metal of these active sites is the first and inevitable step of the ORR. Consequently, we compare the stability against metal leaching in three models, including clean, O-species terminated, and $O_2$ adsorbed $MnN_4$ and $FeN_4$ sites, as shown in Figures 5 and S22.

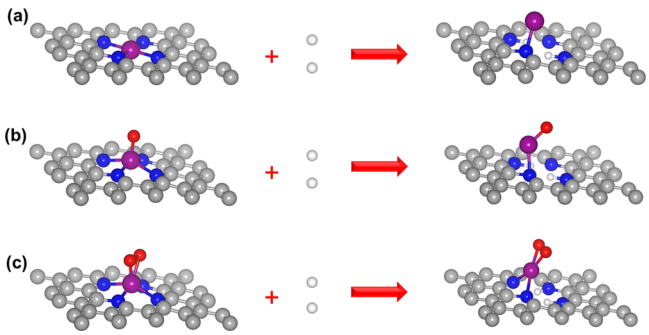


**Figure 5.** Atomistic models showing the leaching of central Mn metal from (a) $MnN_4$ site, (b) oxygen-terminated $MnN_4$ site, and (c) $O_2$ adsorbed $MnN_4$ site. In the figure, the gray, blue, purple, red, and white balls represent C, N, Mn, O, and H atoms, respectively.

As shown in Figure 5, we assume that the change of free energy could gauge the tendency of metal leaching from a metal−$N_4$ site when two protons replace the central atom and hence loses its four N coordination. The free energy change for these processes can be calculated by comparing the energies before and after the metal leaching and considering the free energy of proton as $1/2H_2$ gas in acid media. Namely, a positive value of the free energy change indicates a barrier, whereas a negative value indicates a spontaneous process for the metal leaching process. We presented our DFT calculation results in Table 1. For clean $MnN_4$ and $FeN_4$ sites, we predict that the metal leaching has a high free energy barrier (2.98 eV for $MnN_4$ and 3.38 eV for $FeN_4$).

**Table 1. Free Energy Changes for the Leaching of the Central Metal Atom from $MnN_4$ and $FeN_4$ Sites Calculated from DFT**

| free energy change (eV) | clean | oxygen species-terminated | oxygen molecule-adsorbed |
|---|---|---|---|
| $MnN_4$ | 2.98 | 1.84 | 0.86 |
| $FeN_4$ | 3.38 | 1.33 | 0.76 |

These results indicate that it is challenging to lose metal from the clean $MnN_4$ and $FeN_4$ sites. Hence, we believe that the metal leaching process from the clean metal−$N_4$ sites might have a negligible impact on the stability of the catalysts, which well explains the insignificant activity loss during the potential cycling in $N_2$ saturated $H_2SO_4$.[6] In contrast, Table 1 shows that the free energy changes for the metal leaching from the oxygen-species (O or OH) terminated and $O_2$ adsorbed $MnN_4$ and $FeN_4$ sites are comparatively lower, suggesting that these two processes would contribute significantly to the observed instability of these catalysts. The oxygen-species terminated $MnN_4$ is about 1.84 eV, more stable than the oxygen-species $FeN_4$ site at 1.33 eV. Also, the $O_2$ adsorbed $MnN_4$ is about 0.86 eV more stable than the oxygen-molecule


https://dx.doi.org/10.1021/acscatal.0c02490
ACS Catal. 2020, 10, 10523−10534

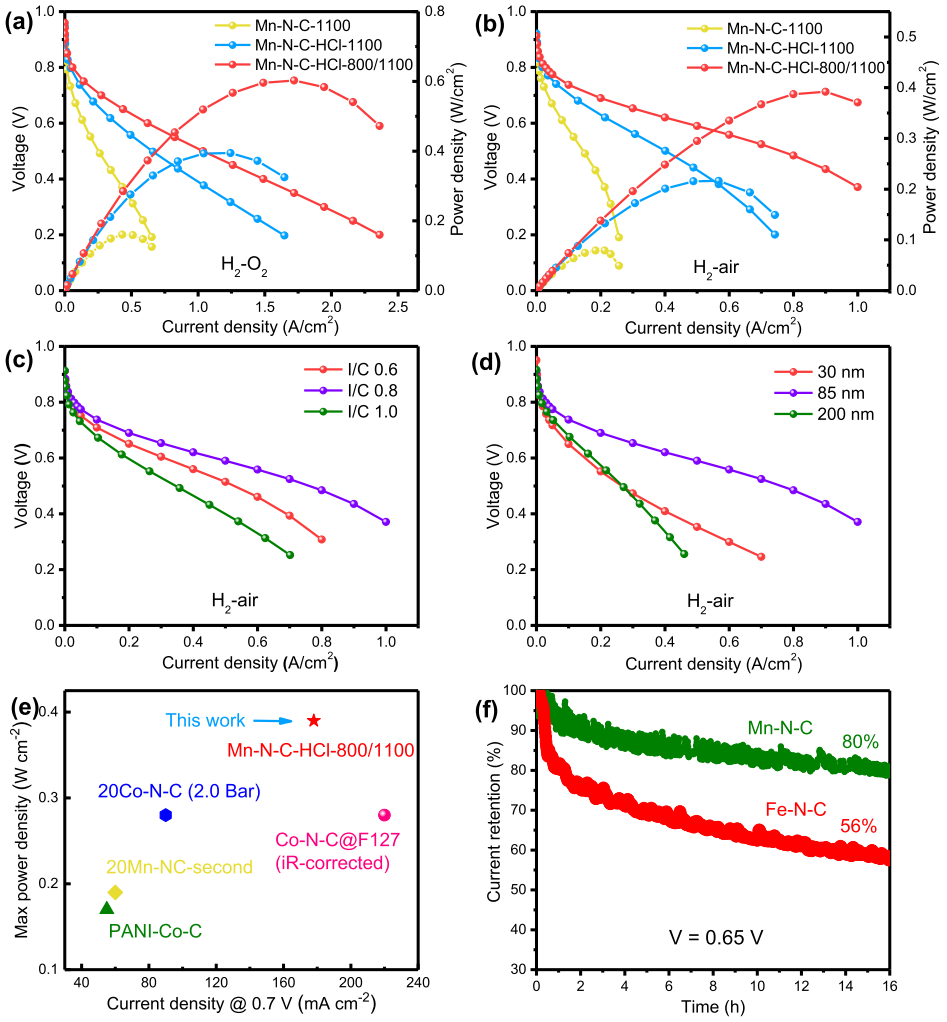


**Figure 6.** (a) Fuel cell performance of different catalysts under $H_2-O_2$. Cathode: 4.0 mg $cm^{-2}$; $O_2$ flow rate 1000 sccm; 100% RH; 1 bar $O_2$ partial pressure; anode: 0.3 $mg_{Pt}$ $cm^{-2}$ Pt/C; $H_2$ flow rate 200 sccm; 100% RH; membrane: Nafion 212. (b) Fuel cell performance of various catalysts under $H_2$-air (1.0 bar). Polarization curves of the best performing Mn−N−C−HCl-800/1100 catalyst with (c) various *I*/*C* ratios and (d) different particle sizes at 100% RH under $H_2$-air conditions. All polarization curves are not *iR* corrected. (e) Comparisons of maximum power density and current density at 0.7 V for reported iron-free cathode catalysts in MEA under $H_2$-air conditions at 80 °C and 100% RH (1.0 bar partial pressure and not *iR* corrected unless specified). (f) Short tem MEA durability tests for Mn−N−C and Fe−N−C catalysts at a constant potential of 0.65 V under $H_2$-air conditions.

adsorbed $FeN_4$ site (0.76 eV). Thus, our DFT calculations provide a mechanistic understanding of the experimentally observed stability improvement of Mn−N−C catalysts as compared to Fe−N−C catalysts.

**2.4. MEA Performance.** Owing to the significant differences in temperature, acidity, pressure, proton/electron conductivity, and electrode structures between RDEs and MEAs, it is challenging to transfer high activities of PGM-free catalysts into MEA performance directly.[7] At first, the fabricated MEA was investigated under the $H_2-O_2$ condition (Figure 6a). As expected, the Mn−N−C-1100 catalyst showed poor performance in the whole current range because of the inferior intrinsic activity of Mn oxides, which also reduced the number of Mn−N active sites and blocked the micropores. Moreover, the Mn−N−C-1100 catalyst showed a tendency to agglomerate together (Figure S23), which can block the dispersion and distribution of ionomer. On the contrary, the performance of the Mn−N−C−HCl-1100 catalyst was improved in the whole current range. However, the Mn−N−C−HCl-1100 catalyst also showed poor mass transport because of insufficient mesopores and macropores, even though particles of the Mn−N−C−HCl-1100 were well-isolated and form less large aggregates. With the step-pyrolysis, the MEA performance of the Mn−N−C−HCl-800/1100 catalyst was significantly improved. It achieved an open circuit voltage (OCV) of 0.95 V, which was comparable to that of our previously reported 20Mn−NC-second catalysts.[20] Meanwhile, the achieved maximum power density of the Mn−N−C−HCl-800/1100 cathode was 0.6 W $cm^{-2}$ under 1.0 bar $O_2$, which was much higher than that of the previous 20Mn−NC-second catalyst (Figure S24). More importantly, the current density at 0.8 V for the Mn−N−C−HCl-800/1100 catalyst was about 1.5 times higher than that of the 20Mn−NC-second catalyst, indicating that more active sites were exposed and utilized under the same condition likely because of the more porous structure of the Mn−N−C−HCl-800/1100 catalyst.

The performance of the catalyst was also investigated under practical $H_2$-air conditions (Figure 6b). Because of the mass transport limitation in the air, the performance gap among the different catalysts became more apparent. The OCV of the


https://dx.doi.org/10.1021/acscatal.0c02490
ACS Catal. 2020, 10, 10523−10534

Mn−N−C−HCl-800/1100 was 0.91 V, which was comparable to other reported iron-free cathode catalysts.[15,20] More importantly, the maximum power density was 0.39 W $cm^{-2}$ under 1.0 bar pressure of $H_2$/air, which is comparable with most Fe-N-C catalysts. The newly achieved power density was two times higher than that of our previously reported 20Mn−NC-second catalysts in 2018 (Figure S24). The curved surface structure likely favors the formation of abundant mesopores/macropores, which enhance the mass transport and improve the utilization of active sites by facilitating ionomer dispersion and distribution.[60] This was verified by microscopy images of MEA structures, where the Mn−N−C−HCl-800/1100 catalyst layer exhibited a porous structure and uniform ionomer distribution. In contrast, large aggregates, dense structure, and high concentrated ionomer were observed for the previous 20Mn−NC-second catalyst layer.

The ratio of ionomer to catalyst was also modulated by preparing MEAs by using the best performing Mn−N−C−HCl-800/1100 catalyst (Figure 6c). The optimal *I*/*C* ratio is determined to be 0.8. The electrochemical surface area of catalysts can be measured to evaluate the number of active sites in contact with ionomer.[61,62] In this study, when the ratio of *I*/*C* was increased from 0.6 to 0.8, both better ionomer coverage of the catalyst and more ionomer infiltration into the catalyst layer were achieved. Thus, the contact area between the catalysts and ionomer was increased accordingly. The $MnN_4$ active sites can participate in the ORR only when they located at the three-phase boundary of the ionomer, oxygen, and carbon. Consequently, the utilization of active sites and the performance of catalysts can be further improved when an optimal *I*/*C* ratio is employed.[22] However, the utilization of catalysts could not be further improved by using excessive ionomer, which only increases the thickness of the ionomer film, leading to high local transport resistance and flooding. In addition, the extra amount of ionomer could block the pores in the electrode. The effect of the primary catalyst size on MEA performance was also studied (Figure 6d). The catalyst with a size of 85 nm demonstrated the best performance due to the uniform distribution of particles in the ink for electrode fabrication (Figure S25), improving the ionomer dispersion and catalyst utilization. Both 30 and 200 nm catalysts showed poor MEA performance. Large aggregates were observed for the 30 nm catalyst, which prohibited the ionomer from infiltrating into the bulk particles. The majority of the ionomer was usually located around the aggregates, and the interior of the catalyst aggregates lacked the ionomer. Even though the 200 nm particles were well-dispersed in the ink, its low ORR activity and low surface area largely limited the MEA performance. Moreover, the thickness of ionomer films would be significantly increased if the primary particle size was increased up to 200 nm, which reduced the mass transport dramatically.[22] Maximum power density and current density at 0.7 V for all reported Fe-free catalysts are summarized in Figure 6e and Table S6.

The MEA durability test of the Mn−N−C−HCl-800/1100 catalyst was also carried out. The cell was tested at a constant voltage of 0.65 V for 160 h. The performance loss is shown in Figure S26, in which 80% activity was retained after the first 16 h, outperforming most of Fe-free cathode catalysts (Table S6). After 100 h, about 50% activity was maintained, demonstrating moderate performance degradation under harsh conditions. The degradation rate was calculated every 20 h (Table S7). The significant performance loss occurred in the first 20 h with a decay rate of 1.26 mA $cm^{-2}$ $h^{-1}$. After around 40 h, the degradation rate became minimal. For comparison, a Fe−N−C catalyst with well-defined $FeN_4$ sites reported by our group was tested under the same condition (Figure 6f).[11] The Fe−N−C catalyst exhibited a much faster degradation rate, which is more than twice that of the Mn catalysts. The fast degradation at the initial phase can be mainly attributed to the metal leaching caused by bond breaking between the metal center and adjacent nitrogen atoms. The much faster degradation of the Fe−N−C catalyst was associated with the fragile nature of the Fe−N bond as elucidated by using DFT studies. Thus, the new Mn−N−C catalyst could be more durable than Fe−N−C catalysts because of the robust nature of $MnN_4$ sites as well as enhanced resistance of carbon corrosion. By comparing the carbon structure of those Mn− and Fe−N−C catalysts, a more predominantly graphitic carbon structure was observed for the Mn−N−C catalyst (Figure S27).

The durability issue is the grand challenge for all M−N−C PGM-free catalysts, especially at high voltages (>0.6 V). The possible causes of M−N−C catalyst degradation were studied in fuel cell cathodes, including the dissolution of $MN_4$ active sites, carbon oxidation, and the collapse of the three-phase boundary.[1] Based on these mechanisms, the correlated efforts should be focused on the enhancement of the M−N bond by modifying the coordination environment and the improvement of carbon supports by increasing the graphitic structure at both atomic and macroscopic levels.[63,64] Moreover, the innovative sphisticated MEA fabrication techniques can mitigate the performance loss by creating robust three-phase interfaces in cathodes.

## 3. CONCLUSIONS

In summary, a new atomically dispersed Mn−N−C PGM-free catalyst was developed by using an aqueous solution synthesis method *via* a two-step doping-adsorption approach. Distinguished from prior studies, the effective acid-assisted aqueous solution method combined with a step-pyrolysis (800 and 1100 °C) enables the formation of a curved surface and highly porous carbon structures in the Mn−N−C catalyst. In addition to low-cost and environmental feasibility, aqueous synthesis leads to an extremely high surface area of the catalyst (1511 $m^2$ $g^{-1}$), which is favorable for hosting atomically dispersed single metal sites.

The atomically dispersed nitrogen-coordinated Mn sites were directly visualized and verified by using HAADF-STEM coupled with EELS at the atomic level. The Mn ions have a +2 valence and are coordinated by four N atoms in the catalyst. The enhanced stability is due to the robust nature of the $MnN_4$ structure and the improved corrosion resistance of its graphitic carbon structure. Additionally, the nature of the stability of $MnN_4$ was elucidated by using DFT calculations, in which $MnN_4$ showed higher resistance to metal leaching than $FeN_4$. The Mn−N−C cathode demonstrated promising fuel cell performance in MEAs. The maximum power density for this catalyst was 0.39 W $cm^{-2}$ under practical $H_2$-air conditions representing the most promising Fe- and PGM-free cathode catalysts. The improved MEA stability of the Mn−N−C catalyst was also observed *via* a constant voltage test under realistic $H_2$-air conditions. Continuous effort is needed to enhance MEA durability by fully elucidating degradation mechanisms, and then developing strategies to strengthen Mn-N bonds and stablize local carbon structures.


https://dx.doi.org/10.1021/acscatal.0c02490
ACS Catal. 2020, 10, 10523−10534

One of the unique features of the Mn−N−C catalyst is the curved surface morphology, which can provide increased external surface and abundant mesopores/macropores. Moreover, the graphitic structure in the catalyst significantly enhances carbon corrosion resistance during the ORR, thus leading to improved stability when compared to other M−N−C catalysts. This work highlights that the atomic $MnN_4$ site catalyst can be prepared from the environmentally benign aqueous solution with improved activity and stability relative to conventional ones synthesized from organic solvents. The atomically dispersed Mn−N−C catalyst, free of Fe and PGMs, holds great promise for future PEMFCs and other advanced electrocatalysis such as $CO_2$ reduction[65] and nitrogen reduction.[66]

## ■ ASSOCIATED CONTENT

### Supporting Information

The Supporting Information is available free of charge at https://pubs.acs.org/doi/10.1021/acscatal.0c02490.

Synthetic procedures, material characterization methods, electrochemical measurements, fuel cell tests, computational methods, and additional electrochemical and physical characterization (PDF)

## ■ AUTHOR INFORMATION


### Corresponding Authors

**Guofeng Wang** − *Department of Mechanical and Materials Engineering, University of Pittsburgh, Pittsburgh, Pennsylvania 15261, United States;* orcid.org/0000-0001-8249-4101; Email: guw8@pitt.edu

**Gang Wu** − *Department of Chemical and Biological Engineering, University at Buffalo, The State University of New York, Buffalo, New York 14260, United States;* orcid.org/0000-0003-0885-6172; Email: gangwu@buffalo.edu

**Hui Xu** − *Giner Inc., Newton, Massachusetts 02466, United States*; Email: hxu@ginerinc.com

### Authors

**Mengjie Chen** − *Department of Chemical and Biological Engineering, University at Buffalo, The State University of New York, Buffalo, New York 14260, United States*

**Xing Li** − *Center for Functional Nanomaterials, Brookhaven National Laboratory, Upton, New York 11973, United States; Key Laboratory of Materials Physics of Ministry of Education, School of Physics and Microelectronics, Zhengzhou University, Zhengzhou 450052, China*

**Fan Yang** − *Giner Inc., Newton, Massachusetts 02466, United States*

**Boyang Li** − *Department of Mechanical and Materials Engineering, University of Pittsburgh, Pittsburgh, Pennsylvania 15261, United States*

**Thomas Stracensky** − *Department of Chemistry and Chemical Biology, Northeastern University, Boston, Massachusetts 02115, United States*

**Stavros Karakalos** − *Department of Chemical Engineering, University of South Carolina, Columbia, South Carolina 29208, United States;* orcid.org/0000-0002-3428-5433

**Sanjeev Mukerjee** − *Department of Chemistry and Chemical Biology, Northeastern University, Boston, Massachusetts 02115, United States*

**Qingying Jia** − *Department of Chemistry and Chemical Biology, Northeastern University, Boston, Massachusetts 02115, United States*

**Dong Su** − *Center for Functional Nanomaterials, Brookhaven National Laboratory, Upton, New York 11973, United States;* orcid.org/0000-0002-1921-6683

Complete contact information is available at: https://pubs.acs.org/10.1021/acscatal.0c02490

### Author Contributions

[▽]M.C., X.L., and F.Y. contributed equally to this work.


### Notes

The authors declare no competing financial interest.

## ■ ACKNOWLEDGMENTS

We are grateful for the financial support from the U.S. Department of Energy, Fuel Cell Technologies Office (DE-EE0008075) and the ElectroCat Consortium. This research used beamline 7-BM (QAS) of the National Synchrotron Light Source II, a U.S. Department of Energy (DOE) Office of Science User Facility operated for the DOE Office of Science by the Brookhaven National Laboratory. The DFT calculations used the computational resources provided by the University of Pittsburgh Center for Research Computing and the Extreme Science and Engineering Discovery Environment (XSEDE) supported by the National Science Foundation grant number ACI-1053575.

## ■ REFERENCES

(1) He, Y.; Liu, S.; Priest, C.; Shi, Q.; Wu, G. Atomically dispersed metal−nitrogen−carbon catalysts for fuel cells: advances in catalyst design, electrode performance, and durability improvement. *Chem. Soc. Rev.* **2020**, *49*, 3484−3524.

(2) Wang, X. X.; Swihart, M. T.; Wu, G. Achievements, challenges and perspectives on cathode catalysts in proton exchange membrane fuel cells for transportation. *Nat. Catal.* **2019**, *2*, 578−589.

(3) Hou, J.; Yang, M.; Ke, C.; Wei, G.; Priest, C.; Qiao, Z.; Wu, G.; Zhang, J. Platinum-group-metal catalysts for proton exchange membrane fuel cells: From catalyst design to electrode structure optimization. *EnergyChem* **2020**, *2*, 100023.

(4) Li, Y.; Wang, H.; Priest, C.; Li, S.; Xu, P.; Wu, G. Advanced Electrocatalysis for Energy and Environmental Sustainability via Water and Nitrogen Reactions. *Adv. Mater.* **2020**, *32*, 2000381.

(5) Lefèvre, M.; Proietti, E.; Jaouen, F.; Dodelet, J.-P. Iron-based catalysts with improved oxygen reduction activity in polymer electrolyte fuel cells. *Science* **2009**, *324*, 71−74.

(6) Wu, G.; More, K. L.; Johnston, C. M.; Zelenay, P. High-Performance Electrocatalysts for Oxygen Reduction Derived from Polyaniline, Iron, and Cobalt. *Science* **2011**, *332*, 443−447.

(7) Chen, M.; He, Y.; Spendelow, J. S.; Wu, G. Atomically Dispersed Metal Catalysts for Oxygen Reduction. *ACS Energy Lett.* **2019**, *4*, 1619−1633.

(8) He, Y.; Tan, Q.; Lu, L.; Sokolowski, J.; Wu, G. Metal-Nitrogen-Carbon Catalysts for Oxygen Reduction in PEM Fuel Cells: Self-Template Synthesis Approach to Enhancing Catalytic Activity and Stability. *Electrochem. Energy Rev.* **2019**, *2*, 231−251.

(9) Wan, X.; Liu, X.; Li, Y.; Yu, R.; Zheng, L.; Yan, W.; Wang, H.; Xu, M.; Shui, J. Fe−N−C electrocatalyst with dense active sites and efficient mass transport for high-performance proton exchange membrane fuel cells. *Nat. Catal.* **2019**, *2*, 259.

(10) Zhang, H.; Chung, H. T.; Cullen, D. A.; Wagner, S.; Kramm, U. I.; More, K. L.; Zelenay, P.; Wu, G. High-performance fuel cell cathodes exclusively containing atomically dispersed iron active sites. *Energy Environ. Sci.* **2019**, *12*, 2548−2558.

(11) Zhang, H.; Hwang, S.; Wang, M.; Feng, Z.; Karakalos, S.; Luo, L.; Qiao, Z.; Xie, X.; Wang, C.; Su, D.; Shao, Y.; Wu, G. Single Atomic Iron Catalysts for Oxygen Reduction in Acidic Media: Particle Size Control and Thermal Activation. *J. Am. Chem. Soc.* **2017**, *139*, 14143−14149.
(12) Martinez, U.; Komini Babu, S.; Holby, E. F.; Chung, H. T.; Yin, X.; Zelenay, P. Progress in the Development of Fe-Based PGM-Free Electrocatalysts for the Oxygen Reduction Reaction. *Adv. Mater.* **2019**, *31*, 1806545.
(13) Asset, T.; Atanassov, P. Iron-Nitrogen-Carbon Catalysts for Proton Exchange Membrane Fuel Cells. *Joule* **2020**, *4*, 33−44.
(14) Wang, X. X.; Prabhakaran, V.; He, Y.; Shao, Y.; Wu, G. Iron-Free Cathode Catalysts for Proton-Exchange-Membrane Fuel Cells: Cobalt Catalysts and the Peroxide Mitigation Approach. *Adv. Mater.* **2019**, *31*, 1805126.
(15) Wang, X. X.; Cullen, D. A.; Pan, Y.-T.; Hwang, S.; Wang, M.; Feng, Z.; Wang, J.; Engelhard, M. H.; Zhang, H.; He, Y. Nitrogen-Coordinated Single Cobalt Atom Catalysts for Oxygen Reduction in Proton Exchange Membrane Fuel Cells. *Adv. Mater.* **2018**, *30*, 1706758.
(16) He, Y.; Hwang, S.; Cullen, D. A.; Uddin, M. A.; Langhorst, L.; Li, B.; Karakalos, S.; Kropf, A. J.; Wegener, E. C.; Sokolowski, J.; Chen, M.; Myers, D.; Su, D.; More, K. L.; Wang, G.; Litster, S.; Wu, G. Highly active atomically dispersed $CoN_4$ fuel cell cathode catalysts derived from surfactant-assisted MOFs: carbon-shell confinement strategy. *Energy Environ. Sci.* **2019**, *12*, 250−260.
(17) Gubler, L.; Dockheer, S. M.; Koppenol, W. H. Radical (HO•, H• and HOO•) formation and ionomer degradation in polymer electrolyte fuel cells. *J. Electrochem. Soc.* **2011**, *158*, B755−B769.
(18) Borup, R.; Meyers, J.; Pivovar, B.; Kim, Y. S.; Mukundan, R.; Garland, N.; Myers, D.; Wilson, M.; Garzon, F.; Wood, D.; Zelenay, P.; More, K.; Stroh, K.; Zawodzinski, T.; Boncella, J.; McGrath, J. E.; Inaba, M.; Miyatake, K.; Hori, M.; Ota, K.; Ogumi, Z.; Miyata, S.; Nishikata, A.; Siroma, Z.; Uchimoto, Y.; Yasuda, K.; Kimijima, K.-i.; Iwashita, N. Scientific Aspects of Polymer Electrolyte Fuel Cell Durability and Degradation. *Chem. Rev.* **2007**, *107*, 3904−3951.
(19) Thompson, S. T.; Wilson, A. R.; Zelenay, P.; Myers, D. J.; More, K. L.; Neyerlin, K. C.; Papageorgopoulos, D. ElectroCat: DOE's approach to PGM-free catalyst and electrode R&D. *Solid State Ionics* **2018**, *319*, 68−76.
(20) Li, J.; Chen, M.; Cullen, D. A.; Hwang, S.; Wang, M.; Li, B.; Liu, K.; Karakalos, S.; Lucero, M.; Zhang, H.; Lei, C.; Xu, H.; Sterbinsky, G. E.; Feng, Z.; Su, D.; More, K. L.; Wang, G.; Wang, Z.; Wu, G. Atomically dispersed manganese catalysts for oxygen reduction in proton-exchange membrane fuel cells. *Nat. Catal.* **2018**, *1*, 935−945.
(21) Liu, K.; Qiao, Z.; Hwang, S.; Liu, Z.; Zhang, H.; Su, D.; Xu, H.; Wu, G.; Wang, G. Mn- and N- doped carbon as promising catalysts for oxygen reduction reaction: Theoretical prediction and experimental validation. *Appl. Catal. B Environ.* **2019**, *243*, 195−203.
(22) Uddin, A.; Dunsmore, L.; Zhang, H.; Hu, L.; Wu, G.; Litster, S. High Power Density Platinum Group Metal-free Cathodes for Polymer Electrolyte Fuel Cells. *ACS Appl. Mater. Interfaces* **2019**, *12*, 2216−2224.
(23) Zhao, X.; Yang, X.; Wang, M.; Hwang, S.; Karakalos, S.; Chen, M.; Qiao, Z.; Wang, L.; Liu, B.; Ma, Q.; Cullen, D. A.; Su, D.; Yang, H.; Zang, H.-Y.; Feng, Z.; Wu, G. Single-Iron Site Catalysts with Self-Assembled Dual-size Architecture and Hierarchical Porosity for Proton-Exchange Membrane Fuel Cells. *Appl. Catal. B Environ.* **2020**, *279*, 119400.
(24) Li, J.; Zhang, H.; Samarakoon, W.; Shan, W.; Cullen, D. A.; Karakalos, S.; Chen, M.; Gu, D.; More, K. L.; Wang, G.; Feng, Z.; Wang, Z.; Wu, G. Thermally Driven Structure and Performance Evolution of Atomically Dispersed FeN 4 Sites for Oxygen Reduction. *Angew. Chem., Int. Ed.* **2019**, *58*, 18971−18980.
(25) Chung, H. T.; Cullen, D. A.; Higgins, D.; Sneed, B. T.; Holby, E. F.; More, K. L.; Zelenay, P. Direct atomic-level insight into the active sites of a high-performance PGM-free ORR catalyst. *Science* **2017**, *357*, 479−484.
(26) Zitolo, A.; Goellner, V.; Armel, V.; Sougrati, M.-T.; Mineva, T.; Stievano, L.; Fonda, E.; Jaouen, F. Identification of catalytic sites for oxygen reduction in iron- and nitrogen-doped graphene materials. *Nat. Mater.* **2015**, *14*, 937−945.
(27) Zhang, H.; Osgood, H.; Xie, X.; Shao, Y.; Wu, G. Engineering nanostructures of PGM-free oxygen-reduction catalysts using metal-organic frameworks. *Nano Energy* **2017**, *31*, 331−350.
(28) Wang, X. X.; Hwang, S.; Pan, Y.-T.; Chen, K.; He, Y.; Karakalos, S.; Zhang, H.; Spendelow, J. S.; Su, D.; Wu, G. Ordered $Pt_3Co$ Intermetallic Nanoparticles Derived from Metal−Organic Frameworks for Oxygen Reduction. *Nano Lett.* **2018**, *18*, 4163−4171.
(29) Mukherjee, S.; Cullen, D. A.; Karakalos, S.; Liu, K.; Zhang, H.; Zhao, S.; Xu, H.; More, K. L.; Wang, G.; Wu, G. Metal-organic framework-derived nitrogen-doped highly disordered carbon for electrochemical ammonia synthesis using $N_2$ and $H_2O$ in alkaline electrolytes. *Nano Energy* **2018**, *48*, 217−226.
(30) Cravillon, J.; Münzer, S.; Lohmeier, S.-J.; Feldhoff, A.; Huber, K.; Wiebcke, M. Rapid room-temperature synthesis and characterization of nanocrystals of a prototypical zeolitic imidazolate framework. *Chem. Mater.* **2009**, *21*, 1410−1412.
(31) Zhang, H.; Li, J.; Tan, Q.; Lu, L.; Wang, Z.; Wu, G. Metal−Organic Frameworks and Their Derived Materials as Electrocatalysts and Photocatalysts for $CO_2$ Reduction: Progress, Challenges, and Perspectives. *Chem.—Eur. J.* **2018**, *24*, 18137−18157.
(32) Crawford, D.; Casaban, J.; Haydon, R.; Giri, N.; McNally, T.; James, S. L. Synthesis by extrusion: continuous, large-scale preparation of MOFs using little or no solvent. *Chem. Sci.* **2015**, *6*, 1645−1649.
(33) Pan, Y.; Liu, Y.; Zeng, G.; Zhao, L.; Lai, Z. Rapid synthesis of zeolitic imidazolate framework-8 (ZIF-8) nanocrystals in an aqueous system. *Chem. Commun.* **2011**, *47*, 2071−2073.
(34) Zhao, X.; Chen, M.; Zuo, J.; Wang, J.; Liu, Z.; Wang, L.; Liu, B.; Wu, G.; Zhang, H.; Yang, H. Fe-Doped Metal-Organic Frameworks-Derived Electrocatalysts for Oxygen Reduction Reaction in Alkaline Media. *J. Electrochem. Soc.* **2018**, *165*, F1278−F1285.
(35) Salunkhe, R. R.; Young, C.; Tang, J.; Takei, T.; Ide, Y.; Kobayashi, N.; Yamauchi, Y. A high-performance supercapacitor cell based on ZIF-8-derived nanoporous carbon using an organic electrolyte. *Chem. Commun.* **2016**, *52*, 4764−4767.
(36) Dissegna, S.; Epp, K.; Heinz, W. R.; Kieslich, G.; Fischer, R. A. Defective Metal-Organic Frameworks. *Adv. Mater.* **2018**, *30*, 1704501.
(37) Vinu, M.; Raja, D. S.; Jiang, Y.-C.; Liu, T.-Y.; Xie, Y.-Y.; Lin, Y.-F.; Yang, C.-C.; Lin, C.-H.; Alshehri, S. M.; Ahamad, T. Effects of structural crystallinity and defects in microporous Al-MOF filled chitosan mixed matrix membranes for pervaporation of water/ethanol mixtures. *J. Taiwan Inst. Chem. Eng.* **2018**, *83*, 143−151.
(38) Wang, H.; Kong, D.; Johanes, P.; Cha, J. J.; Zheng, G.; Yan, K.; Liu, N.; Cui, Y. $MoSe_2$ and $WSe_2$ Nanofilms with Vertically Aligned Molecular Layers on Curved and Rough Surfaces. *Nano Lett.* **2013**, *13*, 3426−3433.
(39) Kibsgaard, J.; Chen, Z.; Reinecke, B. N.; Jaramillo, T. F. Engineering the surface structure of $MoS_2$ to preferentially expose active edge sites for electrocatalysis. *Nat. Mater.* **2012**, *11*, 963.
(40) Cheng, P.; Hu, Y. H. $H_2O$-functionalized zeolitic Zn (2-methylimidazole) 2 framework (ZIF-8) for $H_2$ storage. *J. Phys. Chem. C* **2014**, *118*, 21866−21872.
(41) Jaouen, F.; Herranz, J.; Lefèvre, M.; Dodelet, J.-P.; Kramm, U. I.; Herrmann, I.; Bogdanoff, P.; Maruyama, J.; Nagaoka, T.; Garsuch, A. Cross-laboratory experimental study of non-noble-metal electrocatalysts for the oxygen reduction reaction. *ACS Appl. Mater. Interfaces* **2009**, *1*, 1623−1639.
(42) Proietti, E.; Jaouen, F.; Lefèvre, M.; Larouche, N.; Tian, J.; Herranz, J.; Dodelet, J.-P. Iron-based cathode catalyst with enhanced power density in polymer electrolyte membrane fuel cells. *Nat. Commun.* **2011**, *2*, 416.
(43) Jaouen, F.; Lefèvre, M.; Dodelet, J.-P.; Cai, M. Heat-treated Fe/N/C catalysts for $O_2$ electroreduction: are active sites hosted in micropores? *J. Phys. Chem. B* **2006**, *110*, 5553−5558.


https://dx.doi.org/10.1021/acscatal.0c02490
ACS Catal. 2020, 10, 10523−10534

(44) Chlistunoff, J. RRDE and voltammetric study of ORR on pyrolyzed Fe/polyaniline catalyst. On the origins of variable Tafel slopes. *J. Phys. Chem. C* **2011**, *115*, 6496−6507.
(45) Li, Y.; Zhou, W.; Wang, H.; Xie, L.; Liang, Y.; Wei, F.; Idrobo, J.-C.; Pennycook, S. J.; Dai, H. An oxygen reduction electrocatalyst based on carbon nanotube−graphene complexes. *Nat. Nanotechnol.* **2012**, *7*, 394.
(46) Holewinski, A.; Linic, S. Elementary mechanisms in electrocatalysis: revisiting the ORR Tafel slope. *J. Electrochem. Soc.* **2012**, *159*, H864−H870.
(47) Qiao, Z.; Hwang, S.; Li, X.; Wang, C.; Samarakoon, W.; Karakalos, S.; Li, D.; Chen, M.; He, Y.; Wang, M.; Liu, Z.; Wang, G.; Zhou, H.; Feng, Z.; Su, D.; Spendelow, J. S.; Wu, G. 3D porous graphitic nanocarbon for enhancing the performance and durability of Pt catalysts: a balance between graphitization and hierarchical porosity. *Energy Environ. Sci.* **2019**, *12*, 2830−2841.
(48) Gupta, S.; Zhao, S.; Wang, X. X.; Hwang, S.; Karakalos, S.; Devaguptapu, S. V.; Mukherjee, S.; Su, D.; Xu, H.; Wu, G. Quaternary FeCoNiMn-Based Nanocarbon Electrocatalysts for Bifunctional Oxygen Reduction and Evolution: Promotional Role of Mn Doping in Stabilizing Carbon. *ACS Catal.* **2017**, *7*, 8386−8393.
(49) Nuithitikul, K.; Srikhun, S.; Hirunpraditkoon, S. Influences of pyrolysis condition and acid treatment on properties of durian peel-based activated carbon. *Bioresour. Technol.* **2010**, *101*, 426−429.
(50) Park, S.-J.; Kim, K.-D. Adsorption Behaviors of $CO_2$ and $NH_3$ on Chemically Surface-Treated Activated Carbons. *J. Colloid Interface Sci.* **1999**, *212*, 186−189.
(51) Xiao, W.; Miao, C.; Yin, X.; Zheng, Y.; Tian, M.; Li, H.; Mei, P. Effect of urea as pore-forming agent on properties of poly (vinylidene fluoride-co-hexafluoropropylene)-based gel polymer electrolyte. *J. Power Sources* **2014**, *252*, 14−20.
(52) Jurkiewicz, K.; Pawlyta, M.; Zygadło, D.; Chrobak, D.; Duber, S.; Wrzalik, R.; Ratuszna, A.; Burian, A. Evolution of glassy carbon under heat treatment: correlation structure−mechanical properties. *J. Mater. Sci.* **2018**, *53*, 3509−3523.
(53) Wen, J.; Zeng, Z.; Yang, L.; Zeng, Q.; Lou, H.; Sheng, H.; Miller, D. J.; Yang, W.; Mao, H.-k. TEM Study of Amorphous Carbon with Fully sp3-Bonded Structure. *Microsc. Microanal.* **2017**, *23*, 2268−2269.
(54) Sharma, S.; Shyam Kumar, C. N.; Korvink, J. G.; Kübel, C. Evolution of Glassy Carbon Microstructure: In Situ Transmission Electron Microscopy of the Pyrolysis Process. *Sci. Rep.* **2018**, *8*, 16282.
(55) Chen, Y.; Ji, S.; Chen, C.; Peng, Q.; Wang, D.; Li, Y. Single-atom catalysts: Synthetic strategies and electrochemical applications. *Joule* **2018**, *2*, 1242−1264.
(56) Xia, D.; Yang, X.; Xie, L.; Wei, Y.; Jiang, W.; Dou, M.; Li, X.; Li, J.; Gan, L.; Kang, F. Direct Growth of Carbon Nanotubes Doped with Single Atomic Fe−$N_4$ Active Sites and Neighboring Graphitic Nitrogen for Efficient and Stable Oxygen Reduction Electrocatalysis. *Adv. Funct. Mater.* **2019**, *29*, 1906174.
(57) Guan, J.; Duan, Z.; Zhang, F.; Kelly, S. D.; Si, R.; Dupuis, M.; Huang, Q.; Chen, J. Q.; Tang, C.; Li, C. Water oxidation on a mononuclear manganese heterogeneous catalyst. *Nat. Catal.* **2018**, *1*, 870−877.
(58) Rana, J.; Kloepsch, R.; Li, J.; Scherb, T.; Schumacher, G.; Winter, M.; Banhart, J. On the structural integrity and electrochemical activity of a $0.5Li_2MnO_3 \cdot 0.5LiCoO_2$ cathode material for lithium-ion batteries. *J. Mater. Chem. A* **2014**, *2*, 9099−9110.
(59) Luo, J.-H.; Hong, Z.-S.; Chao, T.-H.; Cheng, M.-J. Quantum Mechanical Screening of Metal-N4-Functionalized Graphenes for Electrochemical Anodic Oxidation of Light Alkanes to Oxygenates. *J. Phys. Chem. C* **2019**, *123*, 19033−19044.
(60) Komini Babu, S.; Chung, H. T.; Zelenay, P.; Litster, S. Resolving electrode morphology's impact on platinum group metal-free cathode performance using nano-CT of 3D hierarchical pore and ionomer distribution. *ACS Appl. Mater. Interfaces* **2016**, *8*, 32764−32777.
(61) Shinozaki, K.; Yamada, H.; Morimoto, Y. Relative humidity dependence of Pt utilization in polymer electrolyte fuel cell electrodes: effects of electrode thickness, ionomer-to-carbon ratio, ionomer equivalent weight, and carbon support. *J. Electrochem. Soc.* **2011**, *158*, B467−B475.
(62) Padgett, E.; Andrejevic, N.; Liu, Z.; Kongkanand, A.; Gu, W.; Moriyama, K.; Jiang, Y.; Kumaraguru, S.; Moylan, T. E.; Kukreja, R. Connecting Fuel Cell Catalyst Nanostructure and Accessibility Using Quantitative Cryo-STEM Tomography. *J. Electrochem. Soc.* **2018**, *165*, F173−F180.
(63) Zhu, Y.; Sokolowski, J.; Song, X.; He, Y.; Mei, Y.; Wu, G. Engineering Local Coordination Environments of Atomically Dispersed and Heteroatom-Coordinated Single Metal Site Electrocatalysts for Clean Energy-Conversion. *Adv. Energy Mater.* **2020**, *10*, 1902844.
(64) Shi, Q.; Hwang, S.; Yang, H.; Ismail, F.; Su, D.; Higgins, D.; Wu, G. Supported and coordinated single metal site electrocatalysts. *Mater. Today* **2020**, *37*, 93−111.
(65) Pan, F.; Zhang, H.; Liu, K.; Cullen, D.; More, K.; Wang, M.; Feng, Z.; Wang, G.; Wu, G.; Li, Y. Unveiling Active Sites of CO2 Reduction on Nitrogen-Coordinated and Atomically Dispersed Iron and Cobalt Catalysts. *ACS Catal.* **2018**, *8*, 3116−3122.
(66) Mukherjee, S.; Yang, X.; Shan, W.; Samarakoon, W.; Karakalos, S.; Cullen, D. A.; More, K.; Wang, M.; Feng, Z.; Wang, G.; Wu, G. Atomically Dispersed Single Ni Site Catalysts for Nitrogen Reduction toward Electrochemical Ammonia Synthesis Using $N_2$ and $H_2O$. *Small Methods* **2020**, *4*, 1900821.


https://dx.doi.org/10.1021/acscatal.0c02490
*ACS Catal.* 2020, 10, 10523−10534